Nicolás García Rosa
Aerodynamics Energetics and Propulsion Department, Institut Supérieur de l'Aéronautique et de l'Espace (ISAE), Université de Toulouse, 10 Avenue, Edouard Belin BP 54032, Toulouse Cedex 4 31055, France
e-mail: Nicolas.Garcia–Rosa@isae.fr

Guillaume Dufour
Aerodynamics Energetics and Propulsion Department, Institut Supérieur de l'Aéronautique et de l'Espace (ISAE), Université de Toulouse, 10 Avenue, Edouard Belin BP 54032, Toulouse Cedex 4 31055, France
e-mail: Guillaume.Dufour@isae.fr

Roger Barènes
Aerodynamics Energetics and Propulsion Department, Institut Supérieur de l'Aéronautique et de l'Espace (ISAE), Université de Toulouse, 10 Avenue, Edouard Belin BP 54032, Toulouse Cedex 4 31055, France
e-mail: Roger.Barenes@isae.fr

Gérard Lavergne
Aerodynamics Energetics and Propulsion Department, Institut Supérieur de l'Aéronautique et de l'Espace (ISAE), Université de Toulouse, 10 Avenue, Edouard Belin BP 54032, Toulouse Cedex 4 31055, France
e-mail: Gerard.Lavergne@isae.fr

Experimental Analysis of the Global Performance and the Flow Through a High-Bypass Turbofan in Windmilling Conditions

A detailed study of the air flow through the fan stage of a high-bypass, geared turbofan in windmilling conditions is proposed, to address the key performance issues of this severe case of off-design operation. Experiments are conducted in the turbofan test rig of ISAE, specifically suited to reproduce windmilling operation in an ambient ground setup. The engine is equipped with conventional measurements and radial profiles of flow quantities are measured using directional five-hole probes to characterize the flow across the fan stage and derive windmilling performance parameters. These results bring experimental evidence of the findings of the literature that both the fan rotor and stator operate under severe off-design angle-of-attack, leading to flow separation and stagnation pressure loss. The fan rotor operates in a mixed fashion: spanwise, the inner sections of the rotor blades add work to the flow while the outer sections extract work and generate a pressure loss. The overall work is negative, revealing the resistive loads on the fan, caused by the bearing friction and work exchange in the different components of the fan shaft. The parametric study shows that the fan rotational speed is proportional to the mass flow rate, but the fan rotor inlet and outlet relative flow angles, as well as the fan load profile, remain constant, for different values of mass flow rate. Estimations of engine bypass ratio have been done, yielding values higher than six times the design value. The comprehensive database that was built will allow the validation of 3D Reynolds-averaged Navier–Stokes (RANS) simulations to provide a better understanding of the internal losses in windmilling conditions.

Keywords: turbofan windmilling, experimental database

1 Context and Motivation

When an aircraft engine flames out during flight, the spools rapidly decelerate and reach a rotational speed maintained by the ram pressure at the inlet. This leads to a stabilized operating condition referred to as windmilling [1]. Windmilling can also occur on air-launched vehicles during the phase prior to launch, when carried by a parent aircraft. In both cases, knowledge of combustor entry pressure, temperature, and mass flow rate is essential to ensure a successful light or relight. More generally, in designing a new engine, the volume of the combustor primary zone is determined to guarantee a minimum in-flight relight envelope after a windmilling phase. Therefore, prediction of key performance parameters in windmilling is crucial for engine designers but also for aircraft and aircraft systems designers. For instance, for multiple-engine aircraft, the resulting drag of the inoperative engine will have an impact on the size of the aircraft vertical stabilizer, required to maintain yaw control in the case of an engine failure at takeoff, and will also affect the glide angle when a landing is attempted. Moreover, the resulting rotational speed will determine how much power may be extracted from the engine, if any, to drive both the engine and the aircraft auxiliary systems.

These parameter values are heavily reliant upon engine architecture and either model predictions or test data are needed at the earliest opportunity. Studies on turbofan windmilling and, more generally, on sub-idle operation, focus on the whole engine by resorting to either Mach number scaling [1], system-level performance modeling [2–6], or experiments [7,8]. To predict the off-design performance, engine models rely on component data (such as compressor maps) which is usually available near the design point, and rarely in severe off-design conditions such as sub-idle or windmilling [2], making it necessary to extrapolate from above-idle data [9]. On the other hand, experiments, usually in altitude test facilities or in flying test beds, are generally expensive and offer a limited number of measurements. Moreover, if the tests are performed in windmilling with the same sensors as in the normal operating range, the gathered data is potentially more uncertain in windmilling than at high engine power [4].

Although this global approach provides essential information on engine performance, it brings no or little insight into the aerodynamics inside the engine. Yet a detailed understanding of the flow features inside the critical components is essential for a reliable prediction of the overall performance, especially in severe off-design operating conditions. Available experimental [10] and numerical studies [10–12] indicate that, in windmilling operation,

the fan stage operates under severe off-design (negative) angle-of-attack conditions, leading to massive flow separation on both the rotor and the stator. However, the most detailed measurements available consider an idealized cascade configuration [10]. Prasad and Lord [12] propose a first analysis of the fan stage behavior by examining engine altitude test data and through numerical simulation. However, no local information is used to validate the flow predictions, suggesting that a detailed measurement of the local flow aerodynamics of a turbofan at windmilling is lacking.

In this context, the Aerodynamics, Energetics, and Propulsion Department of ISAE has developed a specific turbofan test facility dedicated to the study of severe off-design operation of a turbofan, using a multifidelity approach. The engine is equipped with both global cycle performance and local flow measurements. Advanced flow characterization techniques, including unsteady measurements, are currently being implemented. One of the main objectives of this platform is to provide reference data for the validation of both 3D Navier–Stokes and system-level numerical models. This paper aims at examining both the global engine performance as well as the flow features through the fan stage to gain a better understanding of the critical phenomena in windmilling operation. Mass flow measurement and bypass ratio determination as well as fan behavior will be discussed in preparation of future parametric studies. Finally, an experimental database is constituted, for the validation of steady numerical simulations. To the author's best knowledge, this is the first experimental study of the local flow characteristics in a turbofan engine in windmilling operation.

2 Experimental Setup

The engine under consideration is an advanced, high-bypass ratio, unmixed flow geared turbofan (Fig. 1), designed for two to four-seater private light aircraft in twin jet configuration, and optimized for a cruise altitude of 4500 m (15,000 ft) and a cruise Mach number of 0.338. Flight envelope extends to 7500 m (25,000 ft) and Mach 0.4. The fan is less than 352 mm in diameter and is driven by a single low-pressure turbine stage. The core engine consists of a centrifugal compressor and a single-stage uncooled high-pressure turbine stage. At maximum power, the core engine rotates at over 52,000 rpm, the fan rotates at 12,000 rpm, and total mass flow rate is less than 13 kg/s. Start-up is ensured by an electrical motor on the high-pressure shaft, which is then used as a generator to power the electrically driven accessories in flight.

The engine is equipped with conventional instrumentation consisting of steady pressure and temperature measurements as depicted in the top part of Fig. 2, along with the standard station nomenclature defined in Ref. [13]. Total pressure and temperature are measured by radial rakes that are distributed azimuthally to

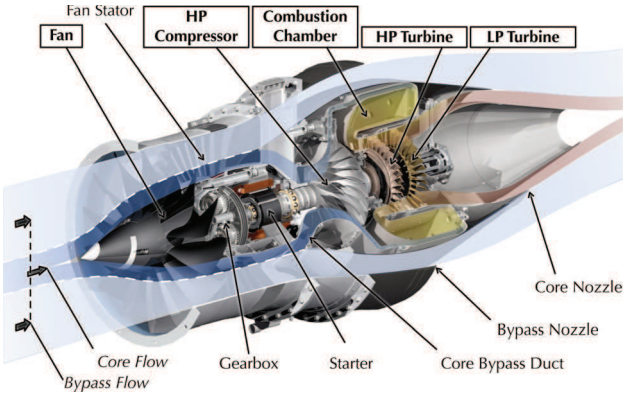

Fig. 1 Architecture of the engine under study at the ISAE test bed. (Photo courtesy of Price Induction.)

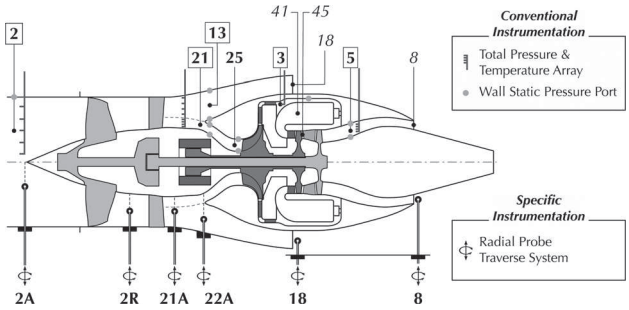

Fig. 2 Engine station nomenclature as per [13], conventional instrumentation and traverse positions

minimize perturbations. Mean values are calculated using mass-weighed averages as per [1]. The associated sensors are permanently mounted, and the data are available throughout the test run with a sampling frequency of 10 Hz. This setup is completed by a set of radial intrusion ports, as shown in the lower part of Fig. 2, allowing the introduction of probes to traverse the cold flow at different azimuthal positions depicted in Figs. 5(*b*), 8(*b*), and 13(*a*). Up to four probes can be traversed simultaneously during one test run, using in-house remotely controlled two-axis positioning systems.

Tests were carried out on the ISAE turbofan test facility, which has been modified to reproduce windmilling conditions at ground level. A 75 kW centrifugal blower is used to blow air through the engine, up to 6 kg/s mass flow rate, yielding a local Mach number of 0.16 at the engine inlet. Figure 3 shows a photo of the experimental setup (Fig. 3(*a*)) as well as a close-up on the engine inlet and part of the instrumentation (Fig. 3(*b*)). For operation, a flexible tube (not on the photo) air-tightly connects the engine to the windmilling blower duct, thus filtering any mechanical vibrations that would otherwise be transmitted from the centrifugal blower to the engine. During windmilling tests, both fuel and oil feeds were cut off, and the engine was only lubricated between test runs.

A parametric study was done by varying the ram pressure at the engine inlet between the minimum and the maximum capacity of the windmilling blower, leading to the operating range presented in Table 1. Several parameters are used to define the windmilling operating point. Flight Mach number M_0 is derived from the ram pressure ratio $p_{i,2}/p_{\text{amb}}$. Mean local Mach number M_2 is derived from the measurements of mean total and static pressure at engine inlet, and flow parameter

$$\Phi_2 = \frac{\dot{m}_2 \sqrt{\mathscr{R} \cdot T_{i,2}}}{p_{i,2} \cdot A_2} \tag{1}$$

is derived from mass flow rate $\dot{m}_2$, which is calculated using flow traverse profiles, as described in Sec. 3.1. The imposed ram pressure ratios lead to values of flight Mach number comprised between 41% and 82% of the nominal flight Mach number of the engine (Table 1), which matches well with what is explored in the literature, on larger engines (see, for example, Refs. [3], [8], and [12]). However, windmilling on the engine under consideration leads to significantly lower values of flow parameter and rotational speeds. Indeed, flow parameter ranges from $\Phi_2 = 0.09$ to 0.38 in the present study while Prasad and Lord [12] explore values from $\Phi_2 = 0.18$ to 0.32, which puts into perspective the comparatively smaller size of the engine under study.

A total of five stabilized points were explored, leading to values of flow parameter of $\Phi_2 = 0.09$, 0.11, 0.13, 0.15, and 0.18. For each stabilized operating point, radial profiles of flow quantities have been done using conventional five-hole probes from Aeroprobe corporation. The L-shaped probe tip is machined from a cone with a half angle of 30 deg and a base diameter of 1.6 mm.

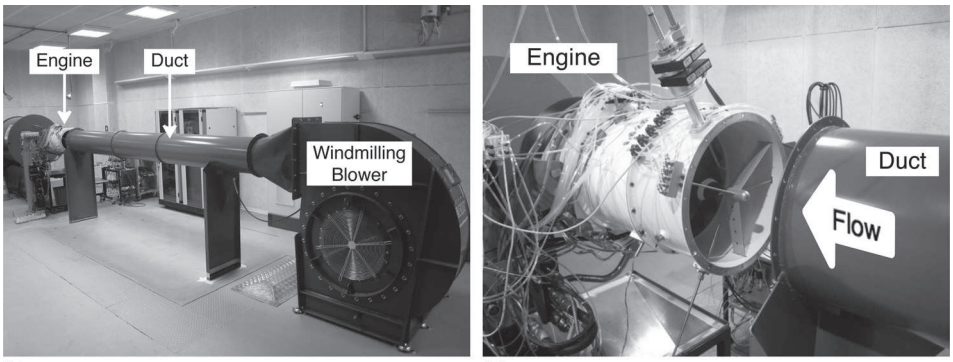

(a) (b)

Fig. 3 Photos of the experimental setup: (*a*) test bed and windmilling fan and (*b*) close-up on the engine

The probes are used with five 0–10 kPa relative pressure transducers accurate to 0.2% full scale (at a 95% uncertainty interval). A miniature thermocouple inserted in the probe head gives access to stagnation temperature. The probes are calibrated at $M = 0.3$ and 0.1 and data reduction is done using the MULTIPROBE software to calculate stagnation pressure, static pressure, as well as flow angles. Since the probes are traversed along different radii of the engine, the probe coordinate system is the local cylindrical coordinate system, therefore, axial, radial and tangential Mach number components (M_x, M_r, M_θ) can be derived. Figure 4 shows the coordinate system and defines the different probe measurements, after data reduction. Flow Mach number M is determined with an uncertainty of 1%, meridional flow angle ψ is determined with an uncertainty of 0.8 deg, and temperature is determined with an absolute uncertainty of 1 K. When probes are installed on the intrusion ports, before a test run, the probe axis $\mathbf{e}_x$ is visually aligned with the engine axis. This leads to systematic initial positioning errors that cause the azimuthal flow angle α to be determined with an uncertainty of 2.8 deg. Finally, since a limited number of probes are available for simultaneous use, for a total of 12 traverse positions, multiple test runs are needed to complete the database. For all our measurements, the repeatability error was found to be smaller than the measurement uncertainty.

3 Flow Field Through the Fan Stage

We first turn our attention to the features of the flow through the fan stage for one selected windmilling operating point, at the maximum inlet Mach number $M_2 = 0.16$ and flow parameter $\Phi_2 = 0.18$. Results are then analyzed to investigate the global fan performance for all the stabilized operating points explored in the database.

3.1 Inlet Flow Field and Mass Flow Rate Measurement. Figure 5 shows the pressure and angle profiles measured for the three available azimuthal positions (B-08, B-09, and B-10) upstream of the fan. Confidence ranges for probe data are marked with gray bands. The good agreement between the three pressure profiles and the azimuthally averaged pressure rake in Fig. 5(*a*) indicates that the inlet distortion is lower than the measurement uncertainty. Angle measurements are perturbed at hub ($\bar{h} = 0$) and shroud ($\bar{h} = 1$) by the proximity of the probe head to the walls and the first and last points of the traverses should be interpreted with caution. However, while the meridional flow angle measurements (Fig. 5(*c*)) suggest an axial flow, the azimuthal angle profiles (Fig. 5(*d*)) exhibit a sensible flow distortion that is generated by the windmilling blower. Indeed, the distance between the engine inlet and the blower, of approximately ten times the duct diameter, is insufficient for the flow to settle into a perfectly axial flow. This distortion is specific to our setup and is found to be repeatable and constant for different values of flow parameter.

Table 1 Operating range of the windmilling facility

Engine parameter		Min.	Max.
Ram pressure ratio	$p_{i,2}/p_{\text{amb}}$	1.014	1.058
Flight Mach number	M_0	0.14	0.28
Inlet Mach number	M_2	0.08	0.16
Mass flow parameter	Φ_2	0.09	0.18
High-pressure shaft rotational speed (% design)	N_{H}	1.4	7.3
Fan rotational speed (% design)	N_{F}	7.75	15.65

While the static pressure profile is uniform, the flow presents a large boundary layer at the shroud, which develops along the 4 m-long duct that links the windmilling blower to the engine. This needs to be taken into account when measuring total mass flow rate and flow parameter Φ_2. For each station, 2A, 2R, 21A, and 22A, the measured Mach number profiles are integrated between hub $R_{\text{h},k}$ and shroud $R_{\text{s},k}$, to calculate the mass flow rate at station k, assuming the flow is azimuthally homogeneous

$$\dot{m}_k = \int_{R_{\text{h},k}}^{R_{\text{s},k}} \frac{p_{i,k}}{\sqrt{\mathscr{R} \cdot T_{i,k}}} \cdot \Phi\left(M_k, M_{x,k}\right) \cdot \left(2\pi \cdot r - \delta_{\theta,k}\right) \mathrm{d}r \qquad (2)$$

where $\delta_{\theta,k}$ is the thickness of a strut that would modify the cross section area at section k and Φ is the mass flow function, defined by

$$\Phi(M, M_x) = \frac{\dot{m}\sqrt{\mathscr{R} \cdot T_i}}{p_i \cdot A} = \sqrt{\gamma} \cdot M_x \cdot \left(1 + \frac{\gamma - 1}{2} M^2\right)^{-\frac{\gamma+1}{2(\gamma-1)}} \qquad (3)$$

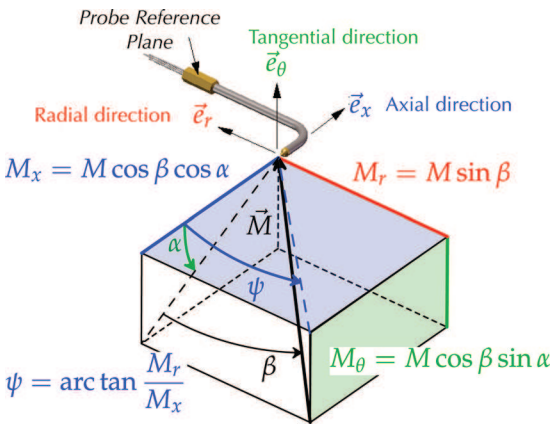

Fig. 4 Five-hole probe measurements

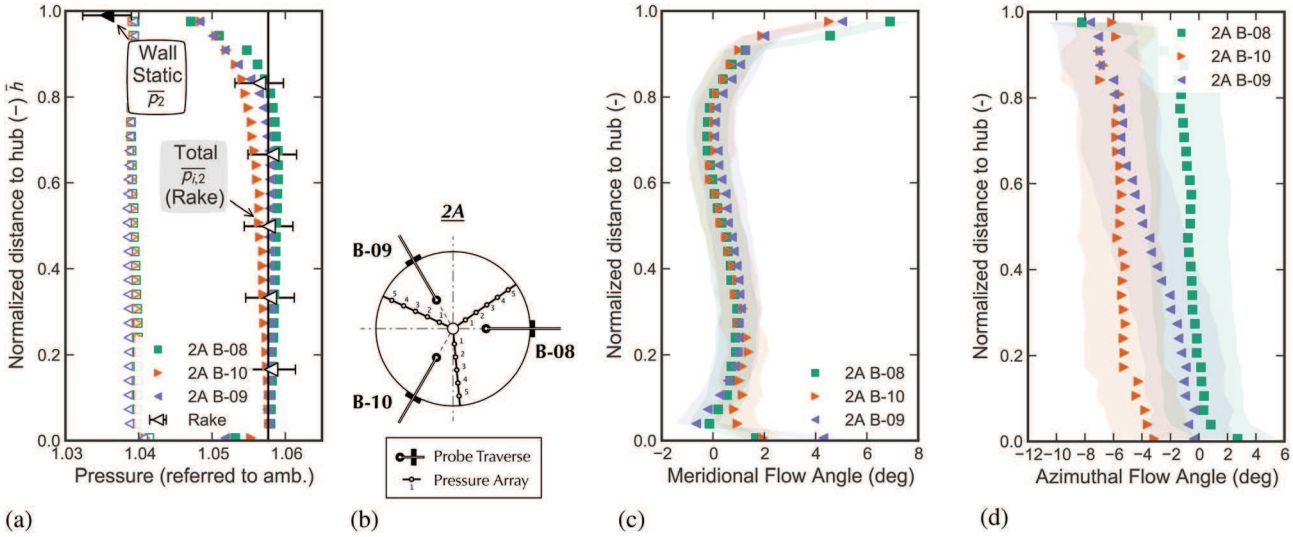

Fig. 5 Radial profiles at engine inlet (station 2A): (*a*) total (▲/▼) and static (△/▽) pressure profiles and (*b*) traverse positions

Flow parameter at engine inlet Φ_k is derived using the mass flow rate m_k obtained at station k and the stagnation conditions at engine inlet, as per Eq. (1). Measurement uncertainty is estimated less than 2.2%.

Figure 6 plots the results versus the nondimensionalized fan tip speed u_t/a, for each measurement station and each stabilized operating point. The error bars show the dispersion of measurements between all the available azimuthal positions of the profile for a given station and therefore show the effect of the azimuthal flow distortion. These results confirm the findings of the literature that a linear relationship exists between fan tip speed and mass flow parameter Φ_2. Experimental results on a larger engine ($\Phi_2 > 0.2$) in Ref. [12] show higher values of fan tip speed lying on a higher slope line, the slope of this line being specific to the geometry of the fan under study and the resistance opposed by the features of the engine (bearing friction and flow through the low-pressure turbine).

The measurements of mean wall static pressure and mean total pressure at engine inlet (shown as $\bar{p}_2$ and $\bar{p}_{i,2}$ in Fig. 5(*a*)) can be used to calculate mean Mach number $\bar{M}_2$ and yield a mean value of flow parameter $\bar{\Phi}_2$, as per Eq. (3). The inlet discharge coefficient, defined as the ratio $C_{D,k} = \Phi_k/\bar{\Phi}_2$ is then calculated for each station, 2A, 2R, 21A, and 22A, and presented in Fig. 7. The results obtained between rotor and stator (station 2R), at stator exit (station 21A) and upstream of the flow splitter (station 22A) can be fitted by a function of the form

$$C_D = \left(1 + B \cdot \Phi_2^n\right)^2 \tag{4}$$

using the values of constants B and n presented in Table 2. The form of this function can be found by considering that the discharge coefficient is also the ratio of the effective cross section $A_2^\star$ to the geometrical cross section A_2, which can in turn be expressed as a function of boundary layer displacement thickness δ_1 to yield the following expression:

$$C_D = \frac{A_2^\star}{A_2} = \left(1 - \frac{\delta_1}{R_{t,2}}\right)^2 \tag{5}$$

Assuming δ_1 is proportional to a Reynolds number to the power n and therefore proportional to Φ_2^n yields the form of Eq. (4). We find that the discharge coefficient estimations using profiles at engine inlet (station 2A) for low values of flow parameter do not conform to this law. This reveals the influence of the azimuthal flow distortion on the estimation of mass flow rate, since the integration of flow profiles assumes the flow is homogeneous. However, this correlation can be used to calculate the value of the flow coefficient in cases where flow profiles are not available.

3.2 Flow Field Through the Fan Stage and Fan Work Coefficient. We now turn our attention to the analysis of the fan stage performance in windmilling. The stagnation pressure profiles at engine inlet (2A), between rotor and stator (2R) and at stator exit (21A) are compared in Fig. 8. For increased readability, only one profile is displayed at engine inlet. Although the measurement uncertainties are higher than the differences we seek to observe, these results suggest a total pressure rise through the rotor (between 2A and 2R), close to the hub ($\bar{h} \lesssim 0.4$). Near the shroud ($\bar{h} \gtrsim 0.4$), a pressure drop is observed, indicating a combination of pressure loss and negative work through the rotor. The comparatively larger pressure drop through the outlet guide vane

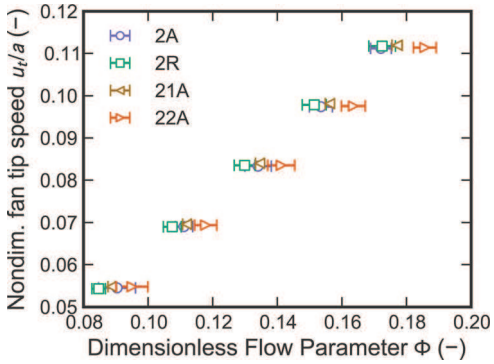

Fig. 6 Nondimensional rotational speed

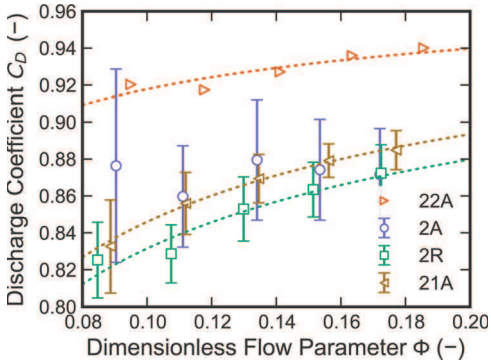

Fig. 7 Inlet discharge coefficient

Table 2 Fit coefficients for Eq. (5)

Station	B	n
2R	0.027	−0.507
21A	0.023	−0.551
22A	0.018	−0.547

(OGV, between 2R and 21A) is consistent with the findings of Prasad and Lord [12] that the bulk stagnation pressure loss occurs in the stator vanes, due to flow separation.

To confirm this observation, the specific work coefficient profile is derived from the application of the Euler turbine equation, using the measurements of azimuthal velocity c_θ and the definitions of Fig. 12(*b*), yielding the following expression:

$$\Psi = \frac{c_p\left(T_{i,2R} - T_{i,2A}\right)}{\frac{1}{2}u_t^2} = \frac{u_2 \cdot \left(c_{\theta,2R} - c_{\theta,2A}\right)}{\frac{1}{2}u_t^2} \tag{6}$$

where u_t is the fan tip speed. Selected profiles of work coefficient are plotted in Fig. 9(*a*). The shapes of the profiles are consistent with the observation that the root of the fan adds work to the fluid and the tip extracts work from the fluid, as the work coefficient is positive near the hub and negative near the shroud. The profiles at different azimuthal positions appear to be shifted and the work coefficient is zero for values of relative height ranging from $\bar{h} \simeq 0.2$ to 0.5. This stems from the uncertainties due to systematic initial probe positioning errors. Indeed, when a probe is moved from an intrusion port to another, it must be visually aligned with the engine axis, which introduces an offset in swirl angle. However, during a test run, all the operating points are measured without repositioning the probes. For instance, Fig. 9(*b*) shows the work profiles obtained at azimuthal position B-03, for the different windmilling operating points. All the profiles collapse to a single curve and the change of behavior is visible at relative height between $\bar{h} \simeq 0.4$ and 0.46. This suggests that, for a given constant level of uncertainty, the overall load on the fan stage is constant as a function of flow parameter. The available profiles are then integrated to calculate the mass-averaged mean value of the work coefficient and the resulting values are plotted versus flow parameter in Fig. 10. All the profiles integrate to negative values, revealing a global energy loss through the fan due to friction on the shaft and load on the low-pressure turbine. As previously discussed, profiles measured at different azimuthal positions (B-01, B-02, B-03) yield different values of global work coefficient due to the initial positioning offset in swirl angle. Yet all positions lead to a constant negative overall work coefficient for the different operating points.

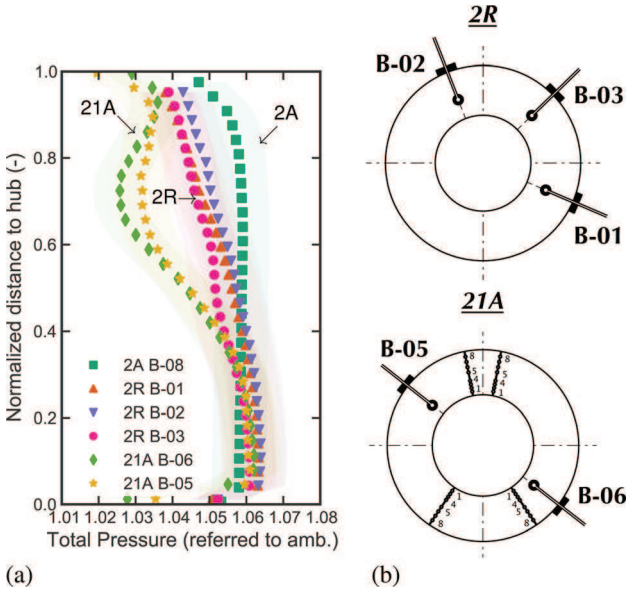

Fig. 8 Radial stagnation pressure profiles through the fan stage: (*a*) pressure profiles and (*b*) traverse positions

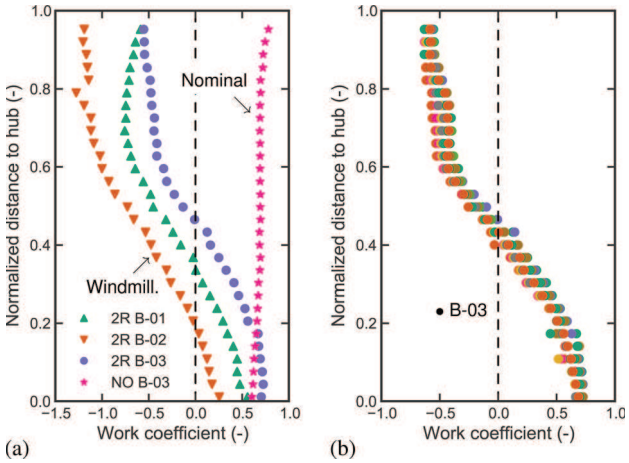

Fig. 9 Fan rotor work coefficient profiles: (*a*) profiles at $\Phi_2 = 0.18$ versus nominal and (*b*) profiles at B-03 for all values of Φ_2

The angle measurements also corroborate this spanwise change in behavior near a normalized height of $\bar{h} \simeq 0.4$. Figure 11 shows the absolute swirl flow angles at stator inlet (Fig. 11(*a*)) and outlet (Fig. 11(*c*)). In windmilling, azimuthal angles are found to be positive near the hub and negative and slightly constant near the shroud and the flow is swirl-free at a normalized height of approximately $\bar{h} \simeq 0.4$. The comparison with normal operation shows the severe off-design angle of attack found in windmilling, which would result in flow separation as pictured in Fig. 11(*b*), and subsequent pressure loss as shown in Fig. 8(*a*). This observation can be attempted in the rotor reference frame. Using the definitions of Fig. 12(*b*) and the measurements of absolute axial and azimuthal velocity components c_x and c_θ, the relative azimuthal flow angle β is calculated using

$$\beta = \arctan\frac{c_\theta - u}{c_x} \tag{7}$$

for rotor inlet (2A) and outlet (2R). The relative angle profiles at inlet, when compared to normal operation (Fig. 12(*a*)), display a severe angle-of-attack operation of the rotor as well, suggesting a flow separation along the rotor blades. The angle difference between windmilling and normal operation is lower than in the case of the stator, which leads to believe that the separation

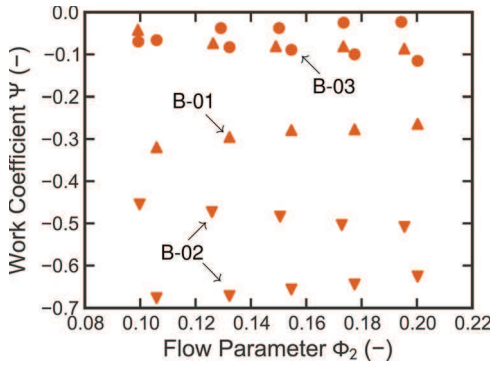

Fig. 10 Fan work coefficient (▲ B-01, ▼ B-02, and • B-03)

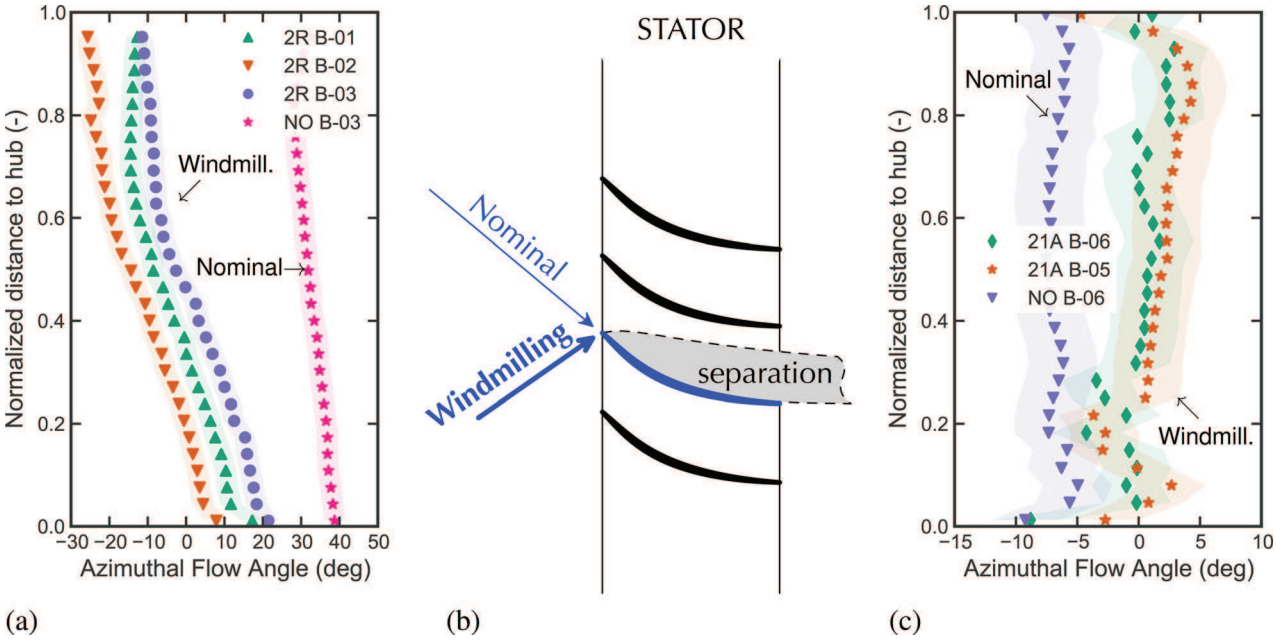

Fig. 11 Absolute azimuthal angles at stator inlet (2R) and outlet (2A): (*a*) stator inlet, (*b*) stator row, and (*c*) stator outlet

phenomena will be less pronounced, as depicted in Fig. 12(*b*). Moreover, results at rotor exit (Fig. 12(*c*)) indicate, as found numerically by Prasad and Lord [12], that the flow exits the rotor at almost the metal angle. Indeed, the relative angle profile at rotor exit in both normal and windmilling operation perfectly match, at the same traverse azimuthal position. Finally, we find that relative angle profiles at inlet and outlet of both rotor and stator collapse to the same curves for different operating points, suggesting that relative angles are independent of mass flow coefficient Φ_2.

3.3 Fan Outlet Guide Vane Exit and Core/Bypass Flow Separation. Further downstream, the flow mixes into a more complex field. The traverse profiles presented in Fig. 13 were measured at less than 3 mm upstream of the core/bypass flow splitter. The geometry of this element can be seen in the meridional view of Fig. 2, at station 22A. The tip of the flow splitter is located at a relative height of $\bar{h} = 0.25$ and is shown on the profiles by a horizontal solid line. The outermost part of the stagnation pressure profiles in Fig. 13(*b*) ($\bar{h} \gtrsim 0.3$) shows that the distortion observed at OGV exit has disappeared, while a large perturbation becomes apparent for $\bar{h} \lesssim 0.3$. This feature originates from the windage in the core duct, leading to the high-pressure compressor. Indeed, static pressure increases and total pressure decreases, resulting in low Mach number levels in the core duct inlet. Additionally, the higher static pressure levels in this region indicate the vicinity of a stagnation point. In the innermost region of the traverse, the low Mach number levels and the close distance of the probe to the splitter and to the structural strut shown in Fig. 13(*a*) cause erroneous measurements that have been removed from the

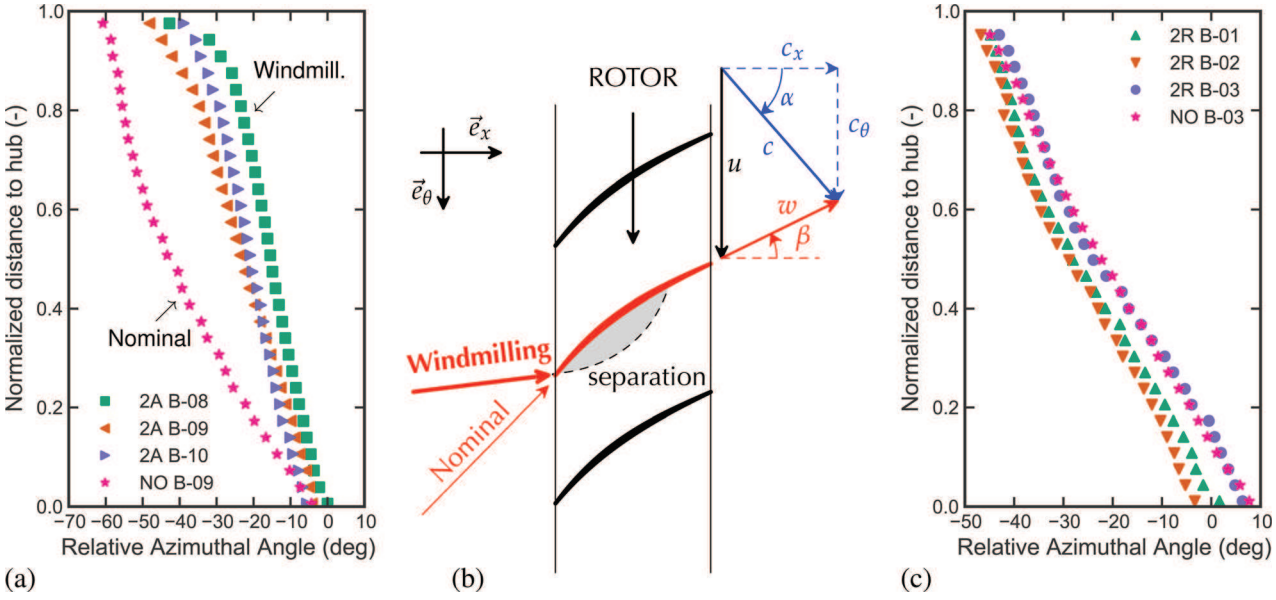

Fig. 12 Relative azimuthal angles at rotor inlet (2A) and outlet (2R): (*a*) rotor inlet, (*b*) rotor row, and (*c*) rotor outlet

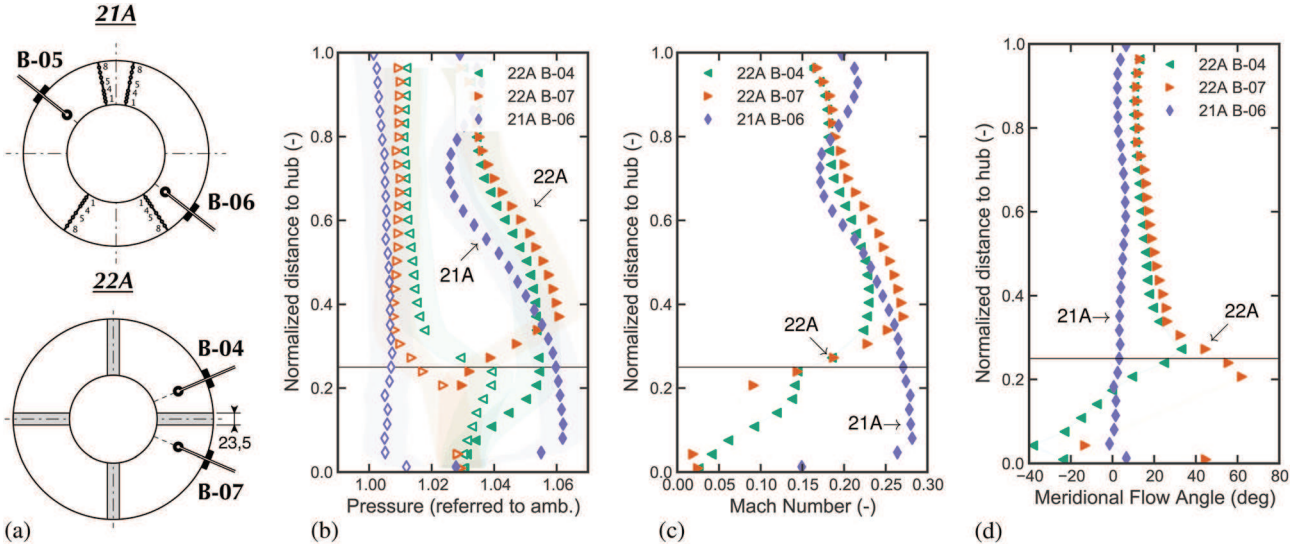

Fig. 13 Radial profiles at stator exit (station 21A) and upstream of the core/bypass flow splitter (station 22A). Empty symbols show static pressure and filled symbols show stagnation pressure: (*a*) traverse positions, (*b*) total (filled symbols), and static (empty symbols) pressure profiles, (*c*) Mach number profile, and (*d*) meridional flow angle profile.

profiles. The fact that these are systematically present in profiles at azimuthal position B-07 and not at position B-04 indicates that the flow is not symmetrical with respect to this strut, suggesting a residual swirl downstream of the stator. Finally, there seems to be flow spillage over the flow splitter, from core to bypass duct, as meridional angle values are positive for $0.15 \lesssim \bar{h} < 0.25$. From this observation, we can imagine the position of the streamline that separates core and bypass flows, as depicted in Fig. 14.

Assuming one can identify the position of this streamline by finding the relative height at which the meridional flow angle is zero, one can place the core/bypass flow separation at approximately $\bar{h} \simeq 0.17$. Integrating the two parts of the axial Mach number profile to derive core ($\bar{h} < 0.17$) and bypass ($\bar{h} > 0.17$) mass flow rates leads to a bypass ratio of 28 for profile B-04 at the reference point ($\Phi_2 = 0.18$). This estimation can be refined using traverse profiles at the core and bypass nozzles. Although total and static pressure levels at the core nozzle exit are very close to ambient pressure, yielding extremely low Mach number levels, these profiles can be integrated to estimate core and bypass mass flow rates, then derive bypass ratio. Results for the five operating points are shown in Fig. 15 and compared to the results of the previously described piecewise integration of profiles at station 22A, assuming two different values of core/bypass separation streamline height, $\bar{h} = 0.13$ and 0.17. The bypass ratio values derived from the nozzle profiles are higher than those derived from profiles at 22A with a separation streamline at $\bar{h} = 0.17$, but results from both stations match if we assume $\bar{h} = 0.13$. This indicates that the separation streamline is actually located closer to the hub, and illustrates the sensitivity to this parameter. Finally, we observe that the bypass ratio scales linearly with flow parameter but appears to level off at larger values of Φ_2.

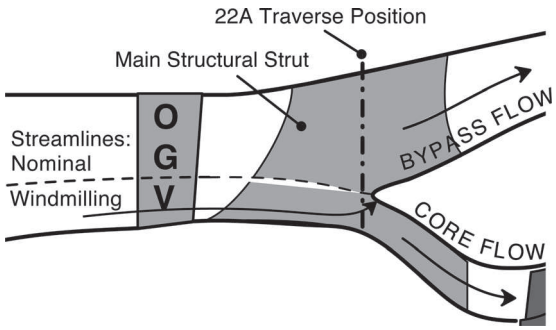

Fig. 14 Streamlines near the flow splitter

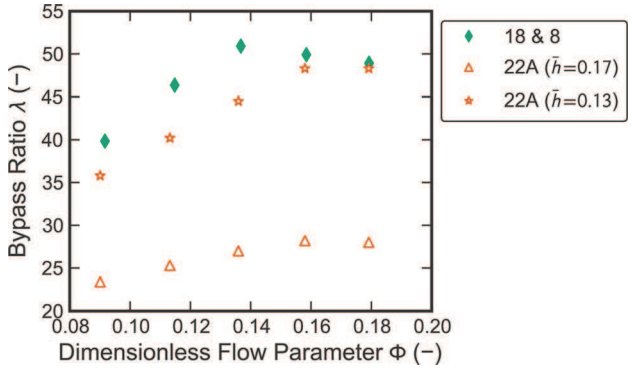

Fig. 15 Windmilling bypass ratio

4 Conclusions

The present study has undertaken an investigation of the behavior of the fan stage of a bypass turbofan in engine-out conditions by reproducing windmilling operation in an atmospheric ground-level test bed. This first experimental database gives an insight into the characteristics of the flow through both fan rotor, stator and near the core/bypass flow splitter, and estimation of key performance parameters of windmilling operation. The results illustrate the difficulties that arise in characterizing the flow in this severe off-design case, given the extremely low pressure and temperature variations. Nonetheless, this work brings experimental evidence confirming important findings, previously reported in the literature, mainly through numerical studies.

The fan is found to operate in severe off-design conditions, with both rotor and stator working under low, sometimes negative values of angle of attack, which leads to flow separation in both rotor and stator vanes. The flow appears to leave the rotor at the same angle as in normal operation, and leave the stator nearly swirl-free. The bulk of the stagnation pressure loss through the fan stage occurs in the stator, due to massive flow separation, and the pressure drop through the rotor is originated by work exchange.

Indeed, the fan rotor operates in a mixed fashion, with the inner 40% of the blade span generating a positive work coefficient, and the outer 60% of the blade span having a negative work coefficient. The spanwise work distribution integrates to different values, depending on the azimuthal position, but for a given position, the global work coefficient remains constant for the different operating points. The overall work is negative, revealing the global resistance the ram flow has to overcome to maintain spool rotation, including bearing friction and an eventual work exchange in the low-pressure turbine. Finally, a strong windage in the core duct is found, leading to complex flow profiles upstream of the core/bypass flow splitter and to values of bypass ratio of over 40, which is more than six times the design value.

Using these results, key performance parameters of windmilling operation were estimated, for different operating points, defined by the dimensionless mass flow coefficient Φ_2. A linear behavior is found for fan tip Mach number, and a correlation was established for the discharge coefficient at fan inlet, as a function of Φ_2. On the other hand, a constant behavior was found in terms of fan relative inlet and outlet flow angles and rotor work coefficient. This leads to believe that these features, along with the complex flows in the rotor and stator vanes, are dependent on the resistive load of the fan, rather than mass flow rate. A good knowledge of bearing friction and potential work exchange with the low-pressure turbine is therefore necessary for the prediction of the fan performance in windmilling.

The gathered data were used in a previous study [5] for the development of a multifidelity approach to windmilling modeling and in Ref. [14] to validate steady-state numerical simulations. This detailed database will allow the validation of RANS numerical simulations to provide better understanding of the complex, 3D flow features across the fan stage, and a more accurate estimation of mass flow rates and bypass ratio. For a more thorough validation, this database needs to be completed with unsteady measurements to characterize the turbulent and unsteady features of the flow, and new traverse positions should be created downstream of the stator, at different azimuthal positions, to characterize the massive flow separation.

Acknowledgment

The engine under consideration is developed by start-up engine manufacturer Price Induction, based in Anglet, France. The authors would like to acknowledge financial support from Snecma and thank Price Induction for providing technical advice, support, and engine data.

Nomenclature

A = speed of sound (m/s)
A_2 = inlet cross section (m^2)
c = absolute velocity (m/s)
c_D = inlet discharge coefficient
c_p = specific heat at constant pressure
$\bar{h}$ = normalized distance to hub
M = Mach number
p = pressure (hPa)
R = radius (m)
$\mathscr{R}$ = ideal gas constant for air (287.04 J/kg K)
T = temperature (K)
u = blade velocity (m/s)
w = relative velocity (m/s)

Greek Symbols

α = swirl flow angle (deg)
β = probe pitch angle (deg)
δ_1 = boundary layer thickness (m)
δ_θ = strut thickness (m)
Φ = dimensionless mass flow parameter
ψ = meridional flow angle (deg)
Ψ = work coefficient

Subscripts

amb = relative to ambient conditions
h = relative to hub
i = relative to stagnation conditions
k = relative to station k = 2A, 2R, 21A, 22A, 8 or 18
s = relative to shroud
t = relative to blade tip
θ = relative to azimuthal component

References

[1] Walsh, P. P., and Fletcher, P., 2004, *Gas Turbine Performance*, Blackwell Science, Oxford, UK.
[2] Anderson, B. A., Messih, D., and Plybon, R., 1997, "Engine Out Performance Characterisitics," 13th International Symposium on Air Breathing Engines (ISABE), 13th, Chattanooga, TN, Sept. 7–12, Paper No. 97-7216.
[3] Braig, W., Schulte, H., and Riegler, C., 1999, "Comparative Analysis of the Windmilling Performance of Turbojet and Turbofan Engines," J. Propul. Power, **15**(2), pp. 326–333.
[4] Riegler, C., Bauer, M., and Schulte, H., 2003, "Validation of a Mixed Flow Turbofan Performance Model in the Sub-Idle Operating Range," ASME Paper No. GT2003-38223.
[5] Pilet, J., Lecordix, J.-L., Garcia Rosa, N., Barènes, R., and Lavergne, G., 2011, "Towards a Fully Coupled Component Zomming Approach in Engine Performance Simulation," ASME Paper No. GT2011-46320.
[6] Fuksman, I., and Sirica, S., 2012, "Real-Time Execution of a High Fidelity Aero-Thermodynamic Turbofan Engine Simulation," ASME J. Eng. Gas Turbines Power, **134**(5), p. 054501.
[7] Wallner, E. E., and Welna, H. J., 1951, "Generalization of Turbojet and Turbine-Propeller Engine Performance in Windmilling Condition," National Advisory Committee for Aeronautics, Washington, DC, Technical Report No. NACA-RM-E51J23.
[8] Mishra, R. K., Gouda, G., and Vedaprakash, B. S., 2008, "Relight Envelope of a Military Gas Turbine Engine: An Experimental Study," ASME Paper No. 2008-43116.
[9] Riegler, C., Bauer, M., and Kurzke, J., 2001, "Some Aspects of Modeling Compressor Behavior in Gas Turbine Performance Calculations," ASME J. Turbomach., **123**(2), pp. 372–378.
[10] Zachos, P. K., Grech, N., Charnley, B., Pachidis, V., and Singh, R., 2011, "Experimental and Numerical Investigation of a Compressor Cascade at Highly Negative Incidence," Eng. Appl. Comput. Fluid Mech., **5**(1), pp. 26–36.
[11] Celestina, M. L., Suder, K. L., and Kulkarni, S., 2010, "Results of an Advanced Fan Stage Over a Wide Operating Range of Speed and Bypass Ratio: Part II—Comparison of CFD and Experimental Results," ASME Paper No. GT2010-44021.
[12] Prasad, D., and Lord, W. K., 2010, "Internal Losses and Flow Behavior of a Turbofan Stage at Windmill," ASME J. Turbomach., **132**(3), p. 031007.
[13] SAE 2004, "Aircraft Propulsion System Performance Station Designation and Nomenclature," SAE, Warrendale, PA, SAE Aerospace Standard SAE-AS755 rev. D.
[14] Dufour, G., Carbonneau, X., and García Rosa, N., 2013, "Nonlinear Harmonic Simulations of the Unsteady Aerodynamics of a Fan Stage Section at Windmill," ASME Paper No. GT2013-95485.